

Intense slow beams of bosonic potassium isotopes

J. Catani^{*,1}, P. Maioli, L. De Sarlo, F. Minardi^{1,2} and M. Inguscio^{1,2}
 LENS - European Laboratory for Non-Linear Spectroscopy and Dipartimento di Fisica,
 Università di Firenze, via N. Carrara 1, I-50019 Sesto Fiorentino - Firenze, Italy
¹INFN, via G. Sansone 1, I-50019 Sesto Fiorentino - Firenze, Italy
²CNR-INFM, via G. Sansone 1, I-50019 Sesto Fiorentino - Firenze, Italy

(Dated: January 23, 2020)

We report on an experimental realization of a two-dimensional magneto-optical trap (2D-MOT) that allows the generation of cold atomic beams of ^{39}K and ^{41}K bosonic potassium isotopes. The high measured fluxes up to 1.0×10^{11} atoms/s and low atomic velocities around 33 m/s are well suited for a fast and reliable 3D-MOT loading, a basilar feature for new generation experiments on Bose-Einstein condensation of dilute atomic samples. We also present a simple multilevel theoretical model for the calculation of the light-induced force acting on an atom moving in a MOT. The model gives a good agreement between predicted and measured flux and velocity values for our 2D-MOT.

PACS numbers: 32.80.Pj, 33.80.Ps, 42.50.Vk, 07.77.Gx, 03.75.Be

I. INTRODUCTION

In the field of atomic physics, experiments and theoretical studies on degenerate mixtures of cold gases have been acquiring a growing interest in the last few years. The vast majority of works have featured Fermi-Bose mixtures, that have now been realized with several combinations of atoms: ^6Li - ^7Li [1], ^6Li - ^{23}Na [2], ^{40}K - ^{87}Rb [3], ^6Li - ^{87}Rb [4]. Many experiments focused on the degenerate Fermi gas, while the bosonic component has only been a tool to reach Fermi degeneracy via sympathetic cooling. Remarkable achievements include BCS-BEC crossover [5, 6, 7, 8, 9, 10], fermionic Bloch oscillations [11], observation of the 3D Fermi surface [12]. Besides, Fermi-Bose systems display a wealth of inter-

esting phenomena genuinely related to the presence of two species. A few, like interspecies Fano-Feshbach resonances [13, 14, 15] and boson-induced collapse of the Fermi gas [16, 17], have already been observed but many more have been proposed and still await experimental confirmation, as e.g. boson-induced superfluidity [18] and mixed phases in optical lattices [19].

On the other hand, Bose-Bose mixtures have remained relatively unexplored: after the pioneering work on ^{41}K - ^{87}Rb [20], to our knowledge only one other double-specie condensate has been recently produced, namely ^{174}Yb - ^{176}Yb [21]. As for the K-Rb mixture, the recent determination of the interspecie scattering length by Feshbach spectroscopy [22] promises a rich phase-diagram for the two species loaded in an optical lattice. In view of an experiment on a K-Rb Bose-Bose mixture we realized and characterized an intense, slow beam of cold bosonic potassium isotopes.

An intense and reliable source of cold atoms represents a favorable starting point for every degenerate mixture experiment. Two-dimensional magneto-optical traps (2D-MOTs) of rubidium have been investigated by several groups [23, 24] and represent one of the brightest sources of slow atoms. With an appropriate double-chamber vacuum system, the 2D-MOT provides high atomic flux through a small aperture between the two chambers. Therefore, it appears perfectly suited for loading an ordinary 3D-MOT in ultra-high vacuum (UHV) environment, the most widely used pre-cooling stage towards quantum degeneracy of dilute gases.

In this work we demonstrate an efficient 2D-MOT for bosonic potassium isotopes ^{39}K and ^{41}K , starting from a natural abundance sample. As a matter of fact, only a 2D-MOT of fermionic ^{40}K has already been implemented [17], while for bosonic isotopes no bright sources have been realized. The peculiarity of bosonic potassium is the tight hyperfine structure of the D_2 line excited state $4^2\text{P}_{3/2}$ [25, 26]: as shown in Fig. 1, the separation between hyperfine levels is comparable to the transition linewidth, $\Gamma = 2\pi \times 6.2$ MHz. This feature represents

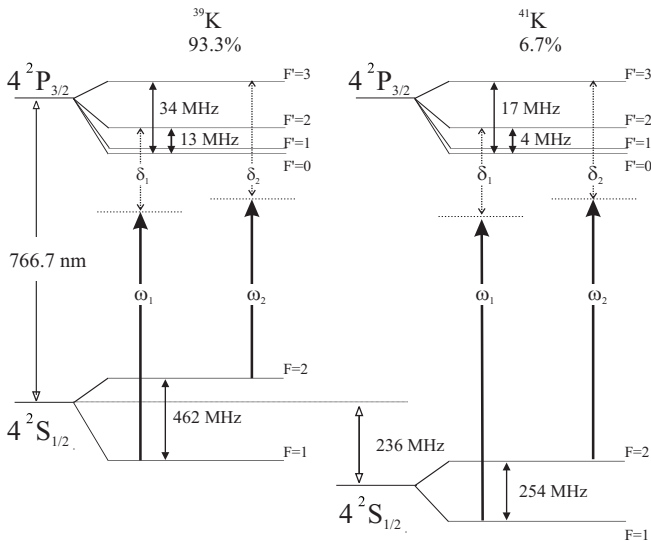


FIG. 1: Level diagrams for ^{39}K and ^{41}K . In the upper part of the diagram is reported the natural abundance of both isotopes.

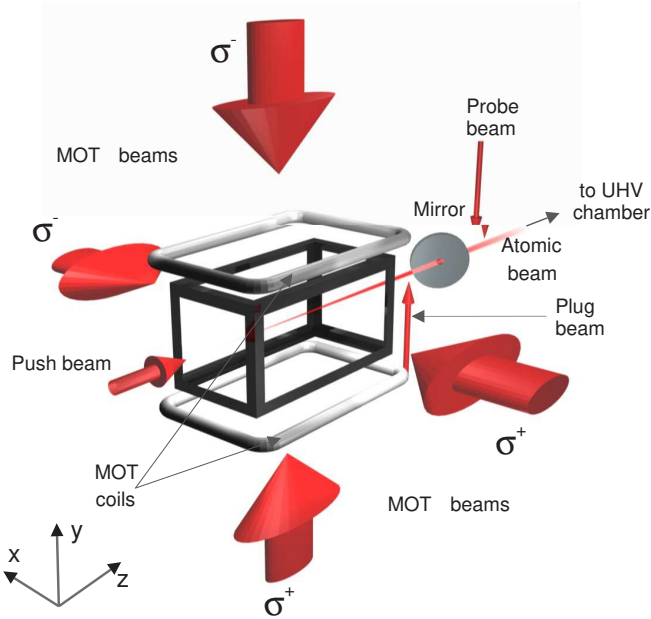


FIG. 2: Schematics of the 2D-MOT system. Two retro-reflected transverse cooling beams, with 3:1 elliptic section, cross in the center of a Ti structure. A pair of copper wired coils generates the quadrupole magnetic field. Near the end of the cell is placed a holed mirror, tilted 45° respect to the longitudinal axis z , along which a 1.5 mm waist push beam is propagating, forcing atoms to travel across the hole. A plug beam is placed near the hole in the mirror, and a probe beam is used to detect the atomic flux in the UHV chamber.

the main physical difference with respect to almost all other alkalis (exception made for Li), and it deeply affects the sub-Doppler cooling mechanism [27]. The aim of the present work is to address the question as to how efficiently 2D-MOT schemes work for bosonic potassium.

The paper is organized as follows. In Sec. II we describe the experimental setup and some experimental techniques used to generate and monitor the cold atomic beam. The results of the characterization of the 2D-MOT are reported in Sec. III, while a theoretical model giving a good reproduction of data is explained in Sec. IV. In Sec. V we conclude with some brief considerations in view of future experiments.

II. EXPERIMENTAL SETUP

A. Vacuum system

The vacuum system consists of two chambers, that we call 2D-MOT and UHV chamber. The 2D-MOT apparatus is schematically reported in Fig. 2. Four rectangular 80×35 mm BK7 anti-reflection coated windows, providing optical access to four transverse trapping beams, are glued on a parallelepipedal metallic structure, machined from a titanium block. The atomic vapor is re-

leased in natural abundance by dispensers, whose injection current controls the pressure in the 2D-MOT chamber. The vacuum setup design gives the possibility to connect to the UHV chamber another identical 2D-MOT chamber. In this scheme it is possible to load a Rb-K mixed 3D-MOT starting from two independently controllable atomic beams.

A flexible, 10 cm long, stainless steel bellow connects the 2D-MOT and the UHV chambers. A metallic mirror, tilted 45° with respect to the longitudinal axis, is placed near the end of the 2D-MOT chamber and close to the bellow. A 1-mm hole is drilled at the center of the mirror to let the atoms exit the 2D-MOT chamber. This mirror allows us to send a hollow beam, counterpropagating with respect to the atoms, so that we can turn to a $2D^+$ -MOT configuration [23].

The 2D-MOT chamber is pumped by a 20 l/s ion diode pump, while in the UHV chamber a 55 l/s ion pump, combined with the tiny conductance of the mirror hole, generates a pressure ratio between the two chambers up to 10^{-4} . Inside the bellow, three graphite tubes of increasing inner diameter (6 to 10 mm) improve the capability of pumping alkali metals.

The quadrupole magnetic field is generated by a pair of 90×40 mm rectangular coils, fixed around the protruding glass windows. This elongated shape yields the required almost 2D axial symmetry to the trapping field. The magnetic gradient in the $x - y$ plane is set to 17 Gauss/cm. The current in each coil is independently adjusted to compensate for stray magnetic fields along the vertical y direction. The compensation of horizontal fields along x is provided by a single large coil, placed far from the chamber. In this configuration, the longitudinal magnetic gradient along z is a factor 10 smaller than in the $x - y$ plane and it will be neglected in the following.

B. Laser system

The cooling and trapping of alkali atoms requires in most cases two laser frequencies which are conventionally called *repumping* and *cooling*. Only the cooling light, tuned to a closed transition, exerts a force upon the atoms, whereas the repumping light is needed only to counteract the hyperfine optical pumping in the ground state, consequent to off-resonant excitation. As such, only a small fraction of the laser power suffices for the repumping light.

The situation is completely different for bosonic potassium, where the tight hyperfine $4^2P_{3/2}$ level spacings are comparable to the natural linewidth Γ . In this case, the cooling transition $|F = 2\rangle \rightarrow |F' = 3\rangle$ is not closed since the $|F' = 1, 2\rangle$ states are excited with similar rates. A fast depletion of the $|F = 2\rangle$ ground state toward the $|F = 1\rangle$ ensues, the repumping light needs to be fairly intense and the cooling force arises from both frequencies [28]. Hence, the distinction between cooling and repumping light makes no sense. However, we will call *repumping*

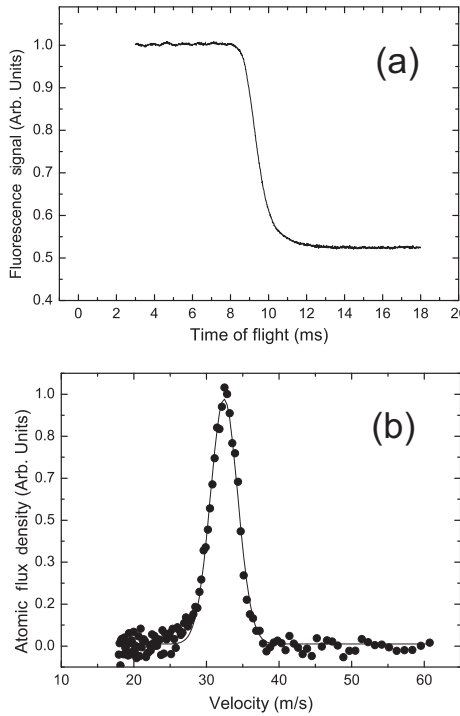


FIG. 3: (a) Typical acquisition of the fluorescence signal. At $t=0$ ms the plug beam is turned on, and after a delay of ~ 8 ms the fluorescence starts decaying to zero. (b) Measured velocity distribution (dots) of atomic beam obtained by a discrete derivative of (a) and gaussian fit to data (solid line). The fitted peak velocity is 32 m/s with a FWHM of 4.5 m/s.

and *cooling* the transitions indicated respectively by ω_1 and ω_2 in Fig. 1.

The ω_1 light is generated by a commercial high-power laser diode with back-emission stabilization grating, providing 400 mW at 767.5 nm. The frequency stabilization is achieved locking this laser by means of modulation-transfer saturation spectroscopy in a reference glass cell containing potassium vapor. To generate the ω_2 radiation, a beam of about 40 mW is split from the laser output, frequency shifted by an acousto-optic modulator (AOM) and then injected into a semiconductor tapered amplifier that delivers 900 mW. In this way, only the repumping laser needs to be frequency locked and the frequency difference between the two sources is precisely set by the radio-frequency signal fed into the AOM. Each of the two main beams is split into several beams with independent amplitude and frequency control.

After a fiber mode-cleaning stage, a pair of cylindrical lenses gives a 3:1 elliptical shape, with a smaller waist of 9.4 mm, to two 2D-MOT transverse beams, which are circularly polarized and retroreflected after the chamber. The maximum laser power for each transverse beam is 50 mW and 80 mW for ω_1 and ω_2 respectively.

Along the z axial direction, we shine an additional σ^+ polarized beam, called *push*, with a waist of 1.5 mm. To achieve the 2D⁺-MOT configuration, a fraction of this

beam is split and directed along the $-z$ direction (*slowing* beam). We recall that the slowing beam has a hollow profile since it enters the 2D-MOT after reflection upon the drilled mirror.

Another vertical 2 mW beam, called *plug*, resonant with the cooling transition, intercepts the atomic flux near the mirror hole: atoms travel unperturbed to the UHV chamber when the plug beam is off and are swept away when the plug beam is on. We use this beam to perform time-of-flight (TOF) measurements, as described below.

C. Detection technique

As in Ref. [23], we analyze the atomic flux by means of TOF fluorescence detection. This is accomplished exposing the atomic flux to a vertical sheet of light (*probe* beam), 30 cm after the mirror hole, and imaging the emitted fluorescence into a broad area photodiode. The peak intensity of the detection beam exceeds 0.5 W/cm², divided between ω_1 and ω_2 , both resonant, in a ratio 1:2.

Switching on the plug beam we interrupt the atomic flux; then, from the analysis of the decaying fluorescence signal $S_F(t)$ as a function of time, we obtain the longitudinal velocity distribution $\rho(v)$ of atoms. Denoting with τ the time required for an atom with velocity v along z to travel the distance L between the plug beam and the detection light sheet, we can write the total flux Φ as:

$$\Phi = \int \rho(v) dv, \quad \text{where} \quad \rho(v) = -\frac{\tau}{\eta} \frac{d}{d\tau} S_F(\tau), \quad (1)$$

with $\tau = L/v$. Here η is an experimental coefficient accounting for the calibration of the photodiode and for the collection solid angle.

Fig. 3(a) shows a typical acquisition of the TOF signal, while the corresponding velocity distribution $\rho(v)$, as derived from Eq. (1), is displayed in Fig. 3(b). To obtain the total atomic flux Φ , the peak velocity and the velocity spread we fit the data with a gaussian function.

III. EXPERIMENTAL RESULTS

We report the measured flux and velocity distribution of ³⁹K and ⁴¹K atomic beams as a function of experimental parameters. We shifted from the first to the second isotope changing the AOMs frequencies and the laser frequency main locking point, preserving the geometrical alignment of the 2D-MOT beams. The analysis on ⁴¹K has been started only after optimization of frequencies and power for the ³⁹K, the former having lower relative abundance (6.7%) than the latter (93.3%).

The region of vapor pressure spanned in the experiment goes from the background pressure to 3.9×10^{-7} mbar, corresponding to the maximum allowed current in the dispenser. We estimate the background gas pressure

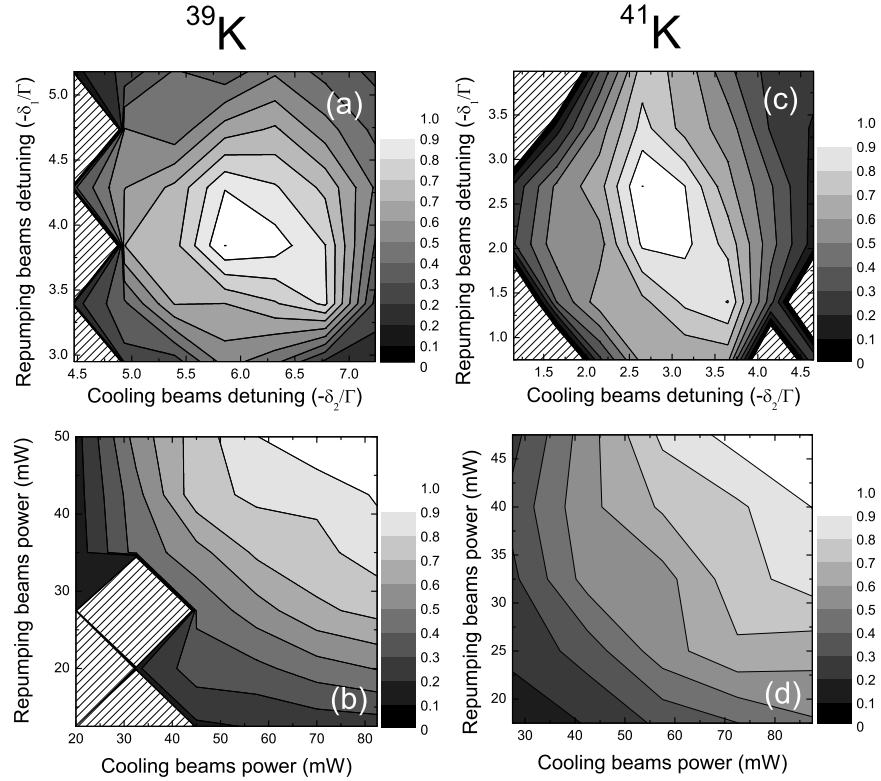


FIG. 4: Measured ^{39}K atomic flux normalized to unity as a function of transverse 2D-MOT beams detuning (a), and of their intensities (b). The detuning values that maximize the atomic flux are $\delta_1 = -3.9\Gamma$ and $\delta_2 = -5.8\Gamma$. In (c) and (d) we report equivalent results obtained for ^{41}K atomic beam, for which the optimal detunings are $\delta_1 = -2.5\Gamma$ and $\delta_2 = -3\Gamma$. No data are taken in the patterned regions.

to be around 10^{-9} mbar. If no differently specified, in the experiment we set the K gas total pressure to 7×10^{-8} mbar.

The divergence of the atomic beam is measured imaging with a CCD camera the fluorescence emitted in the $-x$ direction. The image profile along z corresponds to the gaussian profile of the short axis of detection light sheet, while the vertical (y direction) image profile is diaphragmed by the mirror hole. From the known width of the probe beam we calibrate the image magnification and therefore measure the size of the atomic beam in the y direction. Given the distance of the probe beam from the mirror hole, we calculate a divergence of (34 ± 6) mrad.

A. Trapping beam parameters

To characterize the 2D-MOT, we first set the intensity of both repumping and cooling 2D-MOT beams to their maximum, respectively 50 and 80 mW per beam. We then make a scan of both frequencies ω_1 and ω_2 , searching for the values that maximize the fluorescence signal, hence the total flux of atoms.

We only present data on the total flux Φ because the

atomic velocities display no significant variations with the 2D-MOT parameters. The measured peak velocities span a range between 28 and 35 m/s, while the typical distribution spread is 4.5 m/s (FWHM). Experimental results for ^{39}K detunings are plotted in arbitrary units normalized to the maximum value in Fig. 4(a). The detunings are throughout defined as follows: $\delta_1 = \omega_1 - \omega_{12}$ and $\delta_2 = \omega_2 - \omega_{23}$, where we denote with $\omega_{F'}$ the atomic transition $|4^2\text{S}_{1/2}, F\rangle \rightarrow |4^2\text{P}_{3/2}, F'\rangle$. Note that for these measurements the push beam contains only the repumping component with a power of 6 mW and frequency $\omega_p = \omega_{12} - 5.2\Gamma$. A more detailed analysis of the push beam features is reported in Sec. III C. The detunings optimizing the atomic flux are $\delta_1 = -3.9\Gamma$ and $\delta_2 = -5.8\Gamma$, which correspond to neither of the two configurations reported in [28]. In that work, a MOT is best loaded with both lasers detuned below all hyperfine components, in a Raman configuration such as $|\delta_2 - \delta_1| = \Delta_{32}$ where $\Delta_{32} = 21$ MHz is the hyperfine separation between the $|F' = 3\rangle$ and $|F' = 2\rangle$ excited levels. Similar results were later confirmed in [29]. We speculate that, since our available beam intensities are a fifth to a tenth those of [28], we are unable to reach such large values of detunings.

Then we fix the detunings and decrease both the cool-

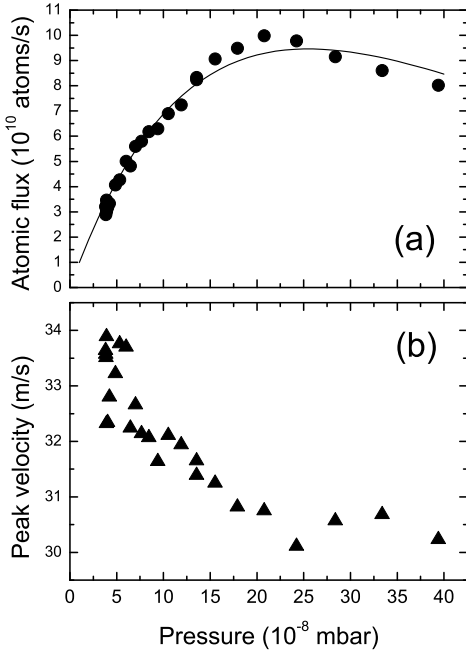


FIG. 5: Measured ^{39}K atomic flux (a) and peak velocity (b) reported as a function of gas pressure in the 2D-MOT chamber. Over the critical value $p = 2.1 \times 10^{-7}$ mbar the atomic flux starts to be depleted by collisional effects. The solid line is a fit obtained using Eq. (3).

ing and repumping beams intensity. Fig. 4(b) shows the ^{39}K atomic flux as a function of the beams intensity: as we see, there are no maxima in the explored range. Thus, an increase of the laser power should make the atomic beam more intense.

The analysis on ^{41}K , is performed along the same lines. Here, the push beam power is set to 6 mW and its frequency to $\omega_p = \omega_{12} - 4.5\Gamma$. Experimental results are plotted in Fig. 4(c, d). As before, while a peak is clearly visible in the frequency dependence of the signal, there is none in the intensity-dependent plot. Even for ^{41}K , more laser power would enhance the number of atoms in the beam.

The largest contribution to the error on the measured total flux comes from the calibration parameter η , more precisely from the evaluation of the solid angle in which fluorescence is collected. We estimate this systematic uncertainty to be 20%, while the statistical error is 5%.

B. Vapor pressure

In order to investigate the dependence of the atomic flux upon the potassium gas pressure, we found convenient to establish a calibration of the vapor pressure p against the dispenser supply current I . This is done prob-

ing the atomic vapor by linear absorption spectroscopy. We simultaneously record the Doppler absorption profiles of the cooling transition in the 2D-MOT chamber and in the reference cell used for laser frequency locking. The pressure of the latter is inferred from its temperature: 2.2×10^{-7} mbar at 43°C . The calibration curve of p as a function of I is well-fit by an exponential: $p = A + \exp(I/I_0 - B)$ with $A = (3.8 \pm 1) \cdot 10^{-8}$ mbar, $I_0 = (0.54 \pm 0.07)$ A and $B = (26.7 \pm 1.8)$.

The maximum allowed current in the dispenser, 6.4 A, sets the highest pressure we reach, i.e. 3.9×10^{-7} mbar. Below the dispenser ignition point, a residual pressure of 4×10^{-8} mbar is likely due to potassium vapor slowly released by the chamber walls.

In Fig. 5(a) we report the measured atomic flux as a function of the pressure for ^{39}K . As we can see, the flux increases with pressure until a critical point and then decreases. In the case of ^{39}K this critical point occurs at $p = 2.1 \times 10^{-7}$ mbar where a flux of 1.0×10^{11} atoms/s is reached. Such a critical point has been observed also for Rb [23, 24, 30] and ascribed to collisions with the background vapor. When the inverse collision rate becomes of the same order of the cooling time t_c , i.e. the time required to reach the mirror hole, the probability for an atom to reach the mirror hole drops. Assuming this is the case also for ^{39}K , we fit our data to obtain the collision rate. The total flux is:

$$\Phi = \int_0^\infty \varphi(t_c) dt_c \quad (2)$$

where $\varphi(t_c)$ is the cooling time distribution.

In the collisionless regime $\varphi(t_c)$ is linearly proportional to the density, hence the pressure, in the 2D-MOT chamber. In presence of collisions with the background vapor, $\varphi(t_c)$ is depleted for $t_c > \gamma$, where $\gamma = \kappa p$ is the collision rate, proportional to the pressure p . Indeed, a single collision with an atom at room temperature ($v_{th} = 250$ m/s) is sufficient to remove the cold atoms from the 2D-MOT velocity capture range. Then, if we assume that the cooling time distribution is a gaussian

$$\varphi(t_c) = \frac{\Phi}{\sqrt{2\pi}\sigma} \exp\left(-\frac{(t_c - t_0)^2}{2\sigma^2}\right),$$

Eq. (2) is modified to

$$\begin{aligned} \Phi &= \int_0^\infty \varphi(t_c) e^{-\gamma t_c} dt_c \\ &= \frac{\Phi}{2} e^{-\gamma t_0 + \gamma^2 \sigma^2 / 2} \left(1 + \text{Erf}\left(\frac{t_0 - \gamma\sigma^2}{\sqrt{2}\sigma}\right) \right), \end{aligned} \quad (3)$$

where $\text{Erf}(x) = \frac{2}{\sqrt{\pi}} \int_0^x \exp(-t^2) dt$ is the usual definition of the error function.

From the numerical simulations illustrated below, we obtain the first and second moment of the cooling time distribution: $t_0 = 5.1$ ms and $\sigma = 1.7$ ms. We then use Eq. (3) to fit the data, with two free parameters:

an overall scaling factor and the collision rate to pressure ratio κ . The results of the fitting is shown by the solid line in Fig. 5(a). The collision rate given by the fit $\gamma(s^{-1}) = (8.6 \pm 0.6) \times p$ (10⁻⁸ mbar) is approximately one order of magnitude larger than the value reported in [31]: 0.3 s⁻¹ at $p = 4 \times (10^{-9}$ mbar, i.e. $0.75 \times p$ (10⁻⁸ mbar). Our value is closer to the collision rates observed with rubidium. A meaningful comparison with Ref. [31] requires a more detailed investigation on the role of light-assisted collisions, assumed negligible for the 2D-MOT.

Another noticeable effect upon pressure increase is the slowing down of the atomic beam, as shown by the plot of the peak velocity in Fig. 5(b). This behavior is in contrast with the case of the simple rubidium 2D-MOT described in [24], where an increase of the gas pressure corresponds to the increase of the peak velocity. Therefore we attribute the observed effect to the progressive absorption of the push beam along its propagation path by the atomic gas since, as reported below, the peak velocity decreases as the push beam intensity is reduced.

As mentioned before, when not otherwise specified all data reported in this work have been taken at $p = 7 \times 10^{-8}$ mbar.

C. Push beam

We turn to the experimental investigation of the atomic beam behavior when the push beam parameters are changed. This is a crucial characterization since we observe no atomic flux in absence of the push beam, in accordance with the findings in experiments with rubidium [23, 24] where the 2D-MOT without push beam is not efficient in our pressure range. Surprisingly, for potassium the push beam works best if one uses only repumping light, and therefore we define the push beam detuning $\delta_p = \omega_p - \omega_{12}$. We defer the discussion of this point to the end of the paragraph.

First we report the atom flux and peak velocity, Figs. 6(a) and 6(b) respectively, for ³⁹K at fixed detuning $\delta_p = -5.2\Gamma$ as a function of power. Above 6 mW, the atom number is approximately constant, while the peak velocity keeps increasing. Therefore, we use a power equal to 6 mW (peak intensity of 170 mW/cm²) in order to have the maximum flux with a velocity distribution still within the capture range of the 3D-MOT in which the atoms will be collected.

No clear enhancements of the flux stem from the addition of a counterpropagating hollow beam along $-z$ direction (2D⁺-MOT configuration). In fact, a 20% reduction in mean velocity was found for a σ^- beam polarization.

Given the hyperfine structure of potassium, one would expect to increase the efficiency of the push force using both cooling and repumping beams, since this avoids the depletion of the ground state population. On the contrary, the atomic beam is deteriorated even by a small fraction of cooling light ω_2 and it is almost extinguished when the ω_2 intensity approaches that of ω_1 . We at-

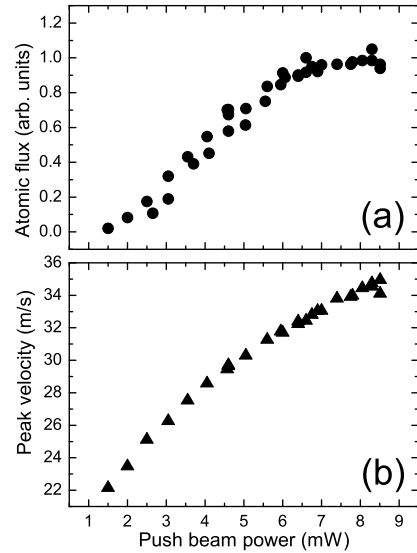


FIG. 6: Atomic flux Φ (a) and peak velocity (b) measured for ³⁹K atomic beam as a function of the push beam power. In this analysis we set $\delta_p = -5.2\Gamma$.

tribute this effect to an increase of both the longitudinal velocity and the radial temperature of the atoms, when pushed by both frequencies. Instead, with a single frequency the hyperfine optical pumping confines the action of the push force within the 2D-MOT volume and the atoms drift freely after the mirror hole.

One may argue that the push beam should then work

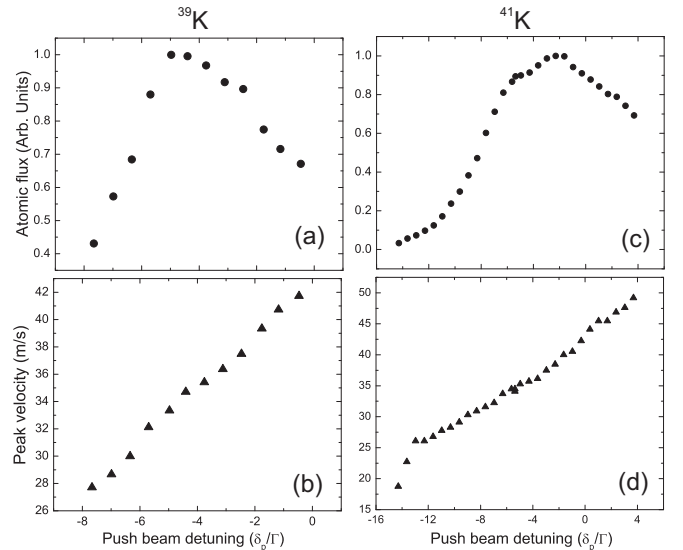


FIG. 7: Measured atomic flux Φ and peak velocity of ³⁹K (a, b) and ⁴¹K (c, d) as a function of the push beam frequency detuning δ_p . The push beam power is set to 6 mW.

TABLE I: Optimal experimental beams power values (P) and detunings (δ) used to generate a cold beam of ^{39}K and ^{41}K atoms. In the right part of the table the total flux Φ values and the corresponding peak velocities are reported. The pressure working point is set to 7×10^{-8} mbar. The magnetic field gradient is 17 Gauss/cm.

Repumping Beams		Cooling Beams		Push Beam		Φ	Peak Velocity
P [mW]	δ_1 [Γ]	P [mW]	δ_2 [Γ]	P [mW]	δ_p [Γ]	[atoms/s]	[m/s]
^{39}K	50	-3.9	80	-5.8	6	-5.2	6.2×10^{10}
^{41}K	47	-2.5	85	-3.0	6	-4.5	5.2×10^9

also with the frequency ω_2 alone. We experimentally find that, at equal power, ω_2 light is far less efficient than ω_1 . We speculate that this is due to ω_2 being more prone to hyperfine optical pumping for two reasons: (i) in the 2D-MOT there is more cooling than repumping light, (ii) ω_2 detuned a few linewidths to the red of the $|F = 2\rangle \rightarrow |F' = 3\rangle$ transition is near to the $|F = 2\rangle \rightarrow |F' = 1, 2\rangle$ resonances causing hyperfine optical pumping (the same effect is less important for the ω_1 light, since the transitions $|F = 1\rangle \rightarrow |F' = 2, 1\rangle$ are closer and there is no hyperfine optical pumping for $|F = 1\rangle \rightarrow |F' = 0\rangle$). Another possible way to avoid hyperfine optical pumping is to use a blue detuned cooling light [32], even if this would increase the pushing efficiency mainly on fast atomic classes and hence confer to the atomic flux a higher peak velocity.

As Fig. 6(a) shows, decreasing the intensity of the laser beam the atomic flux decreases as well. In the pure 2D-MOT configuration, when no push beam is shone on atoms, no flux is detected, independently on both power and frequency of transverse beams and quadrupole magnetic field gradients.

D. Summary

In Tab. I are summarized all the experimental parameters which maximize the total atomic flux Φ of the two isotopes and the values of the corresponding fluxes. For $p = 7 \times 10^{-8}$ mbar high atomic fluxes are achieved, containing 6.2×10^{10} atoms/s and 5.2×10^9 atoms/s for ^{39}K and ^{41}K respectively. The pressure value and their small peak velocities, respectively 35 and 33 m/s, are perfectly adequate to an efficient subsequent loading in a UHV environment 3D-MOT. By increasing p up to 2.1×10^{-7} mbar a flux of 1.0×10^{11} atoms/s of ^{39}K is then observed. A gain of a factor 2 is expected for ^{41}K flux as well at the same value of pressure p .

The high intensity of atomic fluxes is an essential point in order to reach a degenerate regime for K isotopes following a double MOT cooling and trapping scheme. At optimal detunings, with a 15 times lower light intensity, we achieve a 3D-MOT loading rate higher than the one reported in [28]. Thus, we conclude that, to generate a cold atomic beam, a 2D-MOT shows a much higher

efficiency when compared to an ordinary 3D-MOT.

IV. A SIMPLIFIED MULTILEVEL THEORETICAL MODEL

To have a quantitative description of our observation we use an extension of the theoretical model discussed in [30]. This model shortcuts the integration of the optical Bloch equation by assuming a heuristic expression of the total force exerted by the different beams, all having the same frequency, on a two-level atom:

$$\mathbf{f} = \frac{\hbar\Gamma}{2} \sum_i \mathbf{k}_i \frac{s_i}{1 + \sum_j s_j}, \quad (4)$$

$$s_j = \frac{I_j}{I_s} \frac{\Gamma^2}{\Gamma^2 + 4(\delta_j - \mathbf{k}_j \cdot \mathbf{v})^2}$$

where i, j denote the beams and $I_s = \pi h c \Gamma / (3\lambda^3)$ is the two-level saturation intensity, equal to 1.8 mW/cm^2 for potassium D_2 line. Authors of Ref. [30] employ this model to analyze a 3D-MOT of Rb with the addition of a push beam. The extension of this treatment to bosonic potassium, because of the narrow upper level structure, requires to take into account all the allowed hyperfine transitions. For this purpose, we introduce the further assumption that forces arising from different transitions add independently. This amounts to consistently disregard coherences among the two $4S_{1/2}$ hyperfine states, however playing no role in the Doppler cooling mechanism. In principle, we should consider even the Zeeman structure of the hyperfine levels; in practice, to reduce the number of transitions contributing to the total force, we calculate the detunings and the line strength in a manner to average out the Zeeman sublevels. For each laser beam i and each transition $|F\rangle \rightarrow |F'\rangle$, we define the average detuning $\Delta_i^{FF'}$ as the center-of-mass of all the Zeeman components weighted by the squared Clebsch-Gordan coefficients $|c(F', m'; 1, \sigma_i, F, m)|^2$, where σ_i denotes the beam polarization (all beams are circularly polarized with the MOT required elicity). This detuning depends linearly on the displacement from the 2D-MOT axis via the magnetic field gradient. We then define the strength of each hyperfine transition:

$$G_i^{FF'} = \frac{\sum_{m,m'} |c(F', m'; 1, \sigma_i, F, m)|^2}{\sum_{F', m, m'} |c(F', m'; 1, \sigma_i, F, m)|^2}.$$

We incorporate hyperfine optical pumping by breaking the force into two parts, due to the cooling and the repumping light, weighted by the relative populations in the $F = 2$ and $F = 1$ ground levels. Therefore, the expression (4) of the total force is generalized as follows:

$$\mathbf{f} = \frac{p_1}{p_1 + p_2} \mathbf{f}_1 + \frac{p_2}{p_1 + p_2} \mathbf{f}_2 \quad (5)$$

$$\mathbf{f}_F = \frac{\hbar\Gamma}{2} \sum_i \mathbf{k}_i \frac{s_{i,F}}{1 + s_F}, \quad F = 1, 2 \quad (6)$$

with

$$s_{i,F} = \frac{I_{i,F}}{2I_s} \sum_{F'} G_i^{FF'} \frac{\Gamma^2}{\Gamma^2 + 4(\delta_{i,F} - \mathbf{k}_i \cdot \mathbf{v} - \Delta_i^{FF'})^2},$$

where $s_F = \sum_j s_j$. Here, $I_{i,1}, I_{i,2}$ are respectively the repumping and cooling intensity of the i -th beam, and δ_1, δ_2 the corresponding detunings as defined earlier. The populations p_1, p_2 are taken as the equilibrium values of the rate equations for the six hyperfine components.

A. Numerical Simulations

A numerical integration of the classical equations of motion yields the phase-space trajectories. We consider only the atoms that, at $t = 0$, lie on the boundary surface S of the 2D-MOT volume, approximated by a rectangular box with sizes equal to the beam diameters. In sampling the velocity-space, the Boltzmann factor is nearly unity for all velocities lying within the 2D-MOT capture range, well below the 250 m/s thermal velocity. From the integration we extract: (i) the fraction φ of the atoms exiting the mirror hole to the atoms entering the 2D-MOT volume, (ii) the longitudinal velocity distribution of the atomic beam, and (iii) the distribution of the cooling time $\varphi(t_c)$, as defined earlier.

To obtain the total flux, we only need to multiply φ by the total number of atoms entering the cooling volume per second, at pressure p and room temperature T :

$$\Phi = \varphi \times S \frac{p}{\sqrt{2\pi m k_B T}}. \quad (7)$$

In our simulation multiple scattering of light and intra-beam atomic collisions are neglected. The collisions with background gas, occurring at rate $\gamma = 60 \text{ s}^{-1}$, are accounted for by weighting each trajectory with a factor $\exp(-\gamma t_c)$ to deplete the tail of atoms with long cooling times t_c . We also select only those atoms flying in a cone 34 mrad wide around the longitudinal axis z .

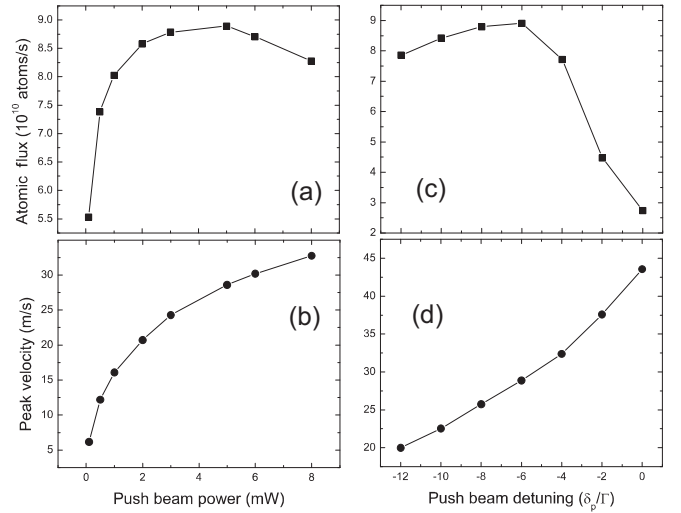


FIG. 8: Results of simulations for ^{39}K : total flux and peak velocity as a function of the push beam power (a,b) and detuning (c,d).

Setting the experimental parameters as in Table I, with a quadrupole magnetic field gradient of 17 Gauss/cm, for ^{39}K we obtain a total flux $\Phi_{\text{sim}} = 8.7 \times 10^{10}$ atoms/s, with a peak velocity of 30.2 m/s, in good agreement with the experimental values reported in Table I.

Repeating the simulation for different values of the push beam power and detuning we find the curves plotted in Fig. 8. The agreement with the experimental findings is satisfactory for the peak velocities. As for the total flux, the model shows saturation in push power at lower values than in the experiment and an optimum detuning of -6Γ close to the observed value of -5.2Γ . The calculated dependence of atomic flux on push beam power and detuning reproduces only qualitatively the experimental curves of Figs. 6(a) and 7(a). We believe that coherent effects ignored in our simulations are likely responsible for the discrepancies with data. A more exact analysis based on the integration of optical Bloch equations is needed to address these issues but is beyond the scope of our simplified model.

V. CONCLUSIONS AND OUTLOOK

The main conclusion of this work is that, similar to rubidium, potassium atoms can be coaxed into an intense and cold beam, still preserving the UHV constraints. Recently, we have used two separate 2D-MOT beams to load a double-specie K/Rb MOT in the UHV chamber as a preliminary step toward quantum degenerate Bose-Bose mixtures. The combination of potassium and rubidium offers a wealth of possibilities to tune the interspecie interactions via Feshbach resonances [22]. Broad Fano-Feshbach resonances are predicted for ^{39}K - ^{87}Rb and ^{41}K - ^{87}Rb in the absolute ground state at 318 G and 515 G,

respectively. For ^{39}K , sympathetic cooling with Rb can be a route to single condensate with tunable interactions, where resonances are expected around 40 G for two atoms in the magnetically trapped state $|F = 1, m = -1\rangle$ [33] and around 20 G for the absolute ground state [34].

An exciting perspective is to tune interactions in presence of an optical lattice, where a rich diagram of insulating and superfluid phases is predicted when the interspecies scattering length is varied [35]. Also, as suggested in [36], entering the Mott-insulator regime for both species paves the way to Feshbach associate long-

lived bosonic heteronuclear molecules, since three-body losses can be suppressed by tayloring the Mott-phase to have one atom per specie in each lattice site.

This work had financial support from Ente Cassa di Risparmio in Firenze and from Istituto Nazionale di Fisica Nucleare through project SQUAT. We warmly thank P. Cladé for his help, G. Modugno for many fruitful suggestions, C. Fort and all the members of the Quantum Degenerate Gas group at LENS for discussions.

[*] E-mail address: catani@lens.unifi.it

[1] F. Schreck, L. Khaykovich, K. L. Corwin, G. Ferrari, T. Bourdel, J. Cubizolles, and C. Salomon, *Phys. Rev. Lett.* **87**, 080403 (2001).

[2] Z. Hadzibabic, C.A. Stan, K. Dieckmann, S. Gupta, M.W. Zwierlein, A. Görlitz, and W. Ketterle, *Phys. Rev. Lett.* **88**, 160401 (2002).

[3] G. Roati, F. Riboli, G. Modugno, and M. Inguscio, *Phys. Rev. Lett.* **89**, 150403 (2002).

[4] C. Silber, S. Günther, C. Marzok, B. Deh, Ph.W. Courteille, and C. Zimmermann, *Phys. Rev. Lett.* **95**, 170408 (2005).

[5] T. Bourdel, L. Khaykovich, J. Cubizolles, J. Zhang, F. Chevy, M. Teichmann, L. Tarruell, S.J.J.M.F. Kokkelmans, and C. Salomon, *Phys. Rev. Lett.* **93**, 050401 (2004).

[6] C. Chin, M. Bartenstein, A. Altmeyer, S. Riedl, S. Jochim, J. Hecker Denschlag, R. Grimm, *Science* **1128**, 305 (2004).

[7] C. A. Regal, M. Greiner, D. S. Jin, *Phys. Rev. Lett.* **92**, 040403 (2004).

[8] G.B. Partridge, K.E. Strecker, R.I. Kamar, M.W. Jack, and R.G. Hulet, *Phys. Rev. Lett.* **95**, 020404 (2005).

[9] J. Kinast, S. L. Hemmer, M. E. Gehm, A. Turlapov, and J.E. Thomas, *Phys. Rev. Lett.* **92**, 150402 (2004).

[10] M. W. Zwierlein, J. R. Abo-Shaeer, A. Schirotzek, C. H. Schunck, and W. Ketterle, *Nature* **435**, 1047 (2005).

[11] G. Roati, E. de Mirandes, F. Ferlaino, H. Ott, G. Modugno, and M. Inguscio, *Phys. Rev. Lett.* **92**, 230402 (2004).

[12] M. Köhl, H. Moritz, T. Stöferle, K. Günter, and T. Esslinger, *Phys. Rev. Lett.* **94**, 080403 (2005).

[13] A. Simoni, F. Ferlaino, G. Roati, G. Modugno, and M. Inguscio, *Phys. Rev. Lett.* **90**, 163202 (2003).

[14] S. Inouye, J. Goldwin, M. L. Olsen, C. Ticknor, J. L. Bohn, and D. S. Jin, *Phys. Rev. Lett.* **93**, 183201 (2004).

[15] C. A. Stan, M.W. Zwierlein, C. H. Schunck, S.M. F. Raupach, and W. Ketterle, *Phys. Rev. Lett.* **93**, 143001 (2004).

[16] G. Modugno, G. Roati, F. Riboli, F. Ferlaino, R. J. Brecha, and M. Inguscio, *Science* **297**, 2240 (2002).

[17] C. Ospelkaus, S. Ospelkaus, K. Sengstock, and K. Bongs, *cond-mat/0507219*.

[18] L. Viverit, C. J. Pethick, and H. Smith, *Phys. Rev. A* **61**, 053605 (2000).

[19] M. Lewenstein, L. Santos, M. A. Baranov, and H. Fehrmann, *Phys. Rev. Lett.* **92**, 050401 (2004).

[20] G. Modugno, M. Modugno, F. Riboli, G. Roati, and M. Inguscio, *Phys. Rev. Lett.* **89**, 190404 (2002).

[21] Y. Takahashi, private communication.

[22] F. Ferlaino, C. D'Errico, G. Roati, M. Zaccanti, M. Inguscio, G. Modugno, and A. Simoni, *cond-mat/0510630* (2005).

[23] K. Dieckmann, R. J. C. Spreeuw, M. Weidemüller, and J. T. M. Walraven, *Phys. Rev. A* **58**, 3891 (1998).

[24] J. Schoser, A. Batär, R. Löw, V. Schweikhard, A. Grabowski, Yu. B. Ovchinnikov, and T. Pfau, *Phys. Rev. A* **66**, 023410 (2002).

[25] E. Arimondo, M. Inguscio, and P. Violino, *Rev. Mod. Phys.* **49**, 31 (1977).

[26] A. Sieradzan, P. Kulatunga, and M. Havey, *Phys. Rev. A* **52**, 4447 (1995).

[27] A. Bambini and A. Agresti, *Phys. Rev. A* **56**, 3040 (1997).

[28] C. Fort, A Bambini, L. Cacciapuoti, F. S. Cataliotti, M. Prevedelli, G. M. L. Tino, and M. Inguscio, *Eur. Phys. J. D* **3**, 113 (1998).

[29] M. Prevedelli, F. S. Cataliotti, E.A. Cornell, J.R. Ensher, C. Fort, L. Ricci, G. M. L. Tino, and M. Inguscio, *Phys. Rev. A* **59**, 886 (1999).

[30] W. Wohlleben, F. Chevy, K. Madison, and J. Dalibard, *Eur. Phys. J. D* **15**, 237 (2001).

[31] R. S. Williamson III, and T. Walker, *J. Opt. Soc. Am. B* **12**, 1393 (1995).

[32] T. B. Swanson, D. Asgeirsson, J. A. Behr, A. Gorelov, and D. Melconian, *J. Opt. Soc. Am. B* **15**, 2641 (1998).

[33] J. L. Bohn, J. P. Burke, C. H. Greene, H. Wang, P. L. Gould, and W. C. Stwalley, *Phys. Rev. A* **59**, 3660 (1999).

[34] E. Tiesinga, private communication.

[35] G.-P. Zheng, J.-Q. Liang, and W. M. Liu, *Phys. Rev. A* **71**, 053608 (2005).

[36] B. Damski, L. Santos, E. Tiemann, M. Lewenstein, S. Kotochigova, P. Julienne, and P. Zoller, *Phys. Rev. Lett.* **90**, 110401 (2003).